ADVANCED ENGINEERING MATERIALS
www.aem-journal.com

Strengthening Nickel by In Situ Graphene Synthesis

*Kaihao Zhang, Matthew Poss, Ping-Ju Chen, and Sameh Tawfick**

Owing to the superior strength and atomic thickness of graphene, it can in theory reinforce metals beyond the usual rule of mixtures bounds by constraining dislocations motion and strain localization at the grain boundaries. This unusual enhancement relies on the graphene's ability to conform to and wrap metal grains. This study experimentally probes the limits of this behavior and investigates the role of interface in designing superior graphene composites. Free-standing nickel–multilayer graphene (Ni–MLG) nanomembranes are fabricated by in situ chemical vapor deposition. Using nanoindentation, elastic modulus (285.16 GPa), maximum stress (2.35 GPa), and toughness (1407.26 Jm^{-2}) are measured, and these values exceed the rule of mixtures bounds. The multi-frequency atomic force microscopy (AFM) is used to spatially map the elastic properties and topography of the MLG on Ni grain boundaries. This emerging characterization reveals that effective reinforcement is achieved when graphene conforms and bridges the grain texture. Nanoindentation and AFM confirm that these mechanisms are ineffective in non-conformally attached Ni–MLG composites, which exhibit significantly weaker mechanical behavior. These results guide the design of effective graphene composites by highlighting the importance of nanoscale roughness and interfaces, and clearly demonstrate the superiority of composite processing routes based on in situ graphene synthesis.

1. Introduction

Graphene is a two-dimensional lattice of sp^2-hybridized carbon atoms arranged in a hexagonal crystal structure. It exhibits superior mechanical, thermal, and electrical transport properties.[1] Specifically, high quality monolayer graphene can have an elastic modulus as high as 1 TPa and strength on the order of 130 GPa.[1a] Nanocrystalline graphene has significantly lower mechanical performance, which can be correlated to the role of grain boundary orientation. Nonetheless, even with sub-optimal properties, graphene has a myriad of potential applications in electric and thermal conductors,[2] corrosion resistant coating,[3] and multi-functional composites.[4] For example, flexible and stretchable electronic materials incorporating graphene are used in wearable sensors, medical diagnostics, and therapeutics, health monitors, and wearable communication devices.[1b] Realization of stretchable conductors relies on the use of electrically conductive graphene,[1b,5] carbon nanotubes (CNTs),[6] or thin metal films having curved designs to accommodate macroscale deformations while locally maintaining small elastic bending strains.[7] Beyond the allowable strain limits, these materials are prone to fracture by unstable crack propagation. In particular, both thin metal films have low toughness and limited mechanical strength due to limited ductility, strain localization, and columnar grain structure.[8] This is also the case for graphene which has high strength but limited toughness.[9] Strong and tough conductive thin metal films therefore have a huge potential to increase the reliability of flexible electronics.

Similarly, applications of graphene in metal matrix composites (MMCs) offer attractive strength, density, and transport properties. One approach to fabricate graphene-MMCs relies on mixing metal powders with reduced graphite oxide (RGO) or graphene nanoplatelets (GPL) by electro deposition or powder metallurgy.[4a,10] It is observed that grapehene segregates to the grain boundaries in these materials. For example, the elastic modulus and the yield strength of 2.5 vol% RGO/Cu composite can be increased by ≈30% and ≈80 % respectively compared to pure Cu.[10b] Notably, a significant portion of this enhancement can be attributed to the role of graphene in confining grain growth during processing, and the observed strength follows the Hall–Petch relation. Another approach relies on mixing metal with polymers such as poly(methyl methacrylate) PMMA, which can be subsequently used as a precursor for in situ graphene growth.[4a,10]

To design effective graphene-metal composites, it is crucial to understand the fundamental strengthening mechanisms governing the behavior of these material systems. It is expected that the interfacial strength between graphene and metals, and the dislocation-graphene interactions at the grain boundaries are the primary factors controlling the extent of reinforcement in graphene-MMC. The interfacial strength of graphene synthesized on thin metal film via chemical vapor deposition (CVD) is found to be 12.8 Jm^{-2} and 72.2 Jm^{-2} for graphene–copper (Gr–Cu) and graphene–nickel (Gr–Ni), respectively.[11] The affinity of graphite basal planes to Ni is well-known, and has been applied to obtain effective load transfer in CNT-Ni MMCs,[12] and incoherent interface systems.[13] The dislocation-grain boundary interaction in the presence of graphene has been carefully studied via layer-by-layer transfer of smooth

Dr. S. Tawfick, K. Zhang, M. Poss, P. J. Chen
Department of Mechanical Science and Engineering, University of Illinois Urbana Champaign, CU 61801, USA
E-mail: tawfick@illinois.edu

DOI: 10.1002/adem.201700475

© 2017 WILEY-VCH Verlag GmbH & Co. KGaA, Weinheim

copper or nickel films and graphene monolayers.[10c,14] By combing in situ SEM experiments with Molecular Dynamics (MD) simulations, it has been shown that graphene–metal composites suppress dislocation motion, which results in strengthening beyond the usual rule of mixture bounds.[14]

In this work, we study the strength and toughness of graphene–metal composites via nanoindentation of free-standing membranes. To isolate the role of the graphene-metal interface, we compare the properties of the CVD-grown Ni-multilayer graphene (referred to as Ni–MLG), to MLG transferred onto Ni (referred to as MLG-on-Ni). We use Amplitude-Modulated Frequency-Modulated Atomic Force Microscopy (AMFM–AFM) to map the spatial distribution of elastic properties and topology of the grapehene-metal interface in the two material systems. We use continuum models to extract the contribution of interfacial energy dissipation on the behavior of metal-graphene composites. We also report the material's electrical conductivity and fracture energy to demonstrate the potential of these films in reliable and defect-tolerant flexible electronics. In addition to specific applications of Ni–MLG composite films, this study emphasizes the effective routes to designing and fabricating strong graphene-metal composites.

2.1. Results and Discussion

2.1. Fabrication of Ni–MLG Composite Nanomenbranes

We sputter thin Ni film on SiO_2/Si substrate ($\approx$1 mm × 3 mm, 300 nm SiO_2) as the template for the subsequent growth of MLG via CVD, as shown in **Figure 1**. As-deposited Ni films with thickness of $\approx$155.2 nm have columnar grain structure with average lateral size of 17.3 nm, as shown in Figure 1a and e and Figure S1a. The as-deposited Ni thin films have surface roughness $\approx$11.6 nm resulting from the sputtering deposition conditions. The Ni films are annealed at 775 °C in 60 sccm of H_2 and 400 sccm of *He* at 1.67 Torr for 30 min. During this step, the native oxide on the Ni surface is reduced while the Ni grains grow in size. The annealing step also decreases the bonding energy of the Ni to the SiO_2 surface and facilitates film delamination. After annealing, graphene is synthesized by flowing 50 sccm of C_2H_4 and 60 sccm of H_2 at 775 °C and 460 mTorr for another 10 min. Following this step, the tube is purged with 600 sccm *He* and the sample is then fast cooled to room temperature by rapidly pulling it out of the tube furnace using a transfer arm. During this cooling step, the carbon atoms segregate out to the surface of Ni film, and multiple layers of graphene nucleate from the Ni grain boundaries and extend to cover the Ni surface.[5] Figure 1**d** shows the surface morphology of these films (referred to as-grown Ni–MLG), where the average grain size increases to about 489 nm (Figure S1b). We use Scanning Electron Microscopy (SEM), Transmission Electron Microscopy (TEM), and Atomic Force Microscopy (AFM) to determine the thickness and topography of the films (Table S2). The thickness of the MLG can be controlled by varying the growth time (1, 5, 10, and 20 min), resulting in thicknesses of 2.6, 7.8, 10.9, and 29.7 nm, respectively. The Ni–MLG interface is uniform, with the MLG showing excellent conformability to the Ni grains as confirmed by TEM image in Figure 1**g**.

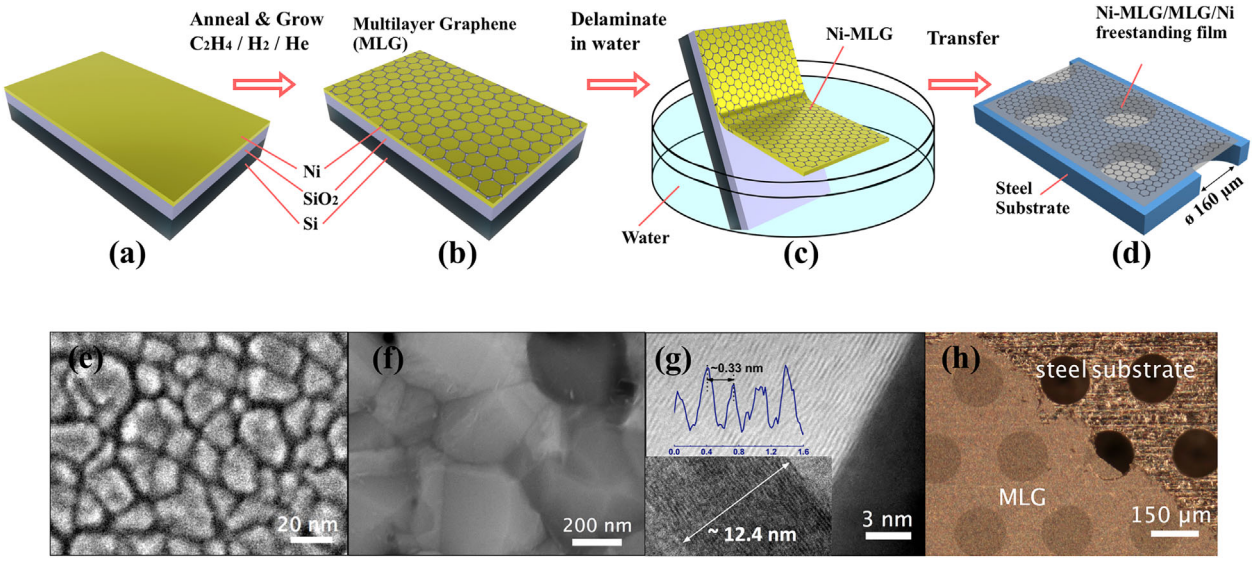

Figure 1. Fabrication of nickel-multilayer graphene (Ni–MLG) composite nanomembranes. a) A thin Ni film is sputtered on SiO_2/Si substrate. b) MLG synthesis is achieved by chemical vapor deposition in $C_2H_4/H_2/He$ gas environment. c) The Ni–MLG thin film can be readily delaminated from SiO_2/Si substrate by floating on the surface of DI water due to the synthesis-induced mechanical stresses. d) The floating Ni–MLG can be transferred onto a stainless steel perforated substrate forming an array of freestanding Ni–MLG membranes (alternatively pristine Ni or MLG films are similarly prepared for testing). e) Scanning Electron Microscopy (SEM) image of as-deposited Ni thin film. f) SEM images of the Ni–MLG thin film composite following synthesis. g) Transmission Electron Microscopy (TEM) images of Ni–MLG interface. h) Optical image of freestanding MLG membranes (after Ni etching by $FeCl_3$/HCl etchant) transferred on a perforated stainless steel substrate with ø = 160 µm holes for nanoindentation.

© 2017 WILEY-VCH Verlag GmbH & Co. KGaA, Weinheim

After synthesis, the Ni–MLG composite films can be readily delaminated from the SiO_2 substrate by slowly submerging it into water. This step is facilitated by the stresses-induced during graphene synthesis.[15] Importantly, the chemical reaction between water molecules and the strained (Si–O–Si) bonds decreases the interfacial energy below the critical adhesion energy, leading to clean and high quality transfer of Ni-based thin film.[16] The floating Ni–MLG film can be transferred onto a perforated steel support substrate (130 μm thick, with ø = 160 μm holes) forming free-standing Ni–MLG circular nanomembranes ready for indentation. We also similarly prepare and test free-standing MLG membranes by exchanging the water with $FeCl_3/HCl$ (Ni etchant) while it is floating and then transferring the MLG film onto the perforated substrate (Figure 1**d and h**). As control samples, we also prepare and test free-standing Ni films after sputtering (referred to as deposited Ni). Finally, we also test Ni films that have been used for MLG synthesis, followed by MLG film removal by reactive O_2 plasma etching (referred to as annealed Ni). We expect that these films have traces of carbon resulting from the graphene synthesis process.

Confocal Raman spectroscopy mapping of 20 × 20 μm areas (Horiba, 532 nm laser at room temperature) was used to characterize the coverage and quality of the MLG in Ni–MLG films and free-standing membranes. As depicted in **Figure 2a**, the as-grown Ni–MLG has G and 2D peaks at 1579 and 2701 cm^{-1}, respectively. The narrow 2D peak (Full Way at Half Maximum (FWHM) ≈55 cm^{-1}) suggests typical orientation misalignment between the graphene layers.[15,17] Notably, after transfer from the growth substrate to the perforated sheets, the free-standing Ni–MLG nanomembranes exhibit slight red-shift (≈5–8 cm^{-1}) in G and 2D peaks which indicate tension in the MLG during the transfer process.[18] The amplitude of the D peak (≈1355 cm^{-1}) suggests some defects introduced during the transfer process.[18a] As shown in Figure 2**b**, the average integrated intensity I_{2D}/I_G and I_D/I_G are ≈0.910 and ≈0.362, respectively, indicating relatively high quality of the nanocrystalline MLG layers.[19]

2.2. Mechanical Behavior Probed by Membrane Nnanoindentation

The mechanical behavior of the composite films is measured by indenting the center of the free-standing circular membranes shown in Figure 1**h** using a spherical diamond indenter of 5 μm diameter and cone angle of 60°. **Figure 3a** shows the typical load-displacement curves of free-standing Ni–MLG membranes, MLG (i.e., Ni etched as described above) and the control experiments with as-deposited Ni and annealed Ni. We carried out extensive nanoindentation studies using loads ranging from 20 to 800 μN, all the way until film facture. Figure S2 shows the loading-unloading behavior of a typical Ni–MLG thin film for peak loads of 20, 30, and 100 μN. Based on the shape of unloading curves, we identified that a load of 20 μN and displacement of ≈1000 nm retains the elastic regime with negligible hysteresis. Notably, intermediate loads demonstrate measureable hysteresis that we attribute to limited Ni plasticity, slip within the MLG,[20] and interfacial slip between Ni and MLG. At high loads, discontinuities in the loading curves, and significant hysteresis can be attributed to nano cracks. We extract the elastic modulus by fitting the load-displacement curves in the elastic regime below 1 μm displacement. In the range where the ratio of tip size to membrane diameter is small $\left(\frac{c}{a} \ll 1\right)$ and the membrane rotation is minimal ($\varphi \approx -\frac{\partial w_0}{\partial r}|_{max} < 0.02$, where w_0 is membrane central deflection, r is radius), we can apply the analytical description of clamped circular membrane under point load and prestrain (due to residual stress in transfer process).[21] A continuum mechanics model capturing both bending- and stretching-dominated behavior can be expressed as follows[1a,21–22]

$$P = \frac{4\pi E h^3}{3(1-\upsilon^2)a^2} w_0 + \frac{2\pi\sigma_0 h}{\ln\left(\frac{a}{c}\right)} w_0 + \frac{Eh}{a^2 f_\upsilon^3} w_0^3 \tag{1}$$

where P and w_0 are the applied load and central deflection, a and c are radius of thin film and indenter tip, h is the thin film thickness, E and υ are elastic modulus and the Poisson's ratio, σ_0

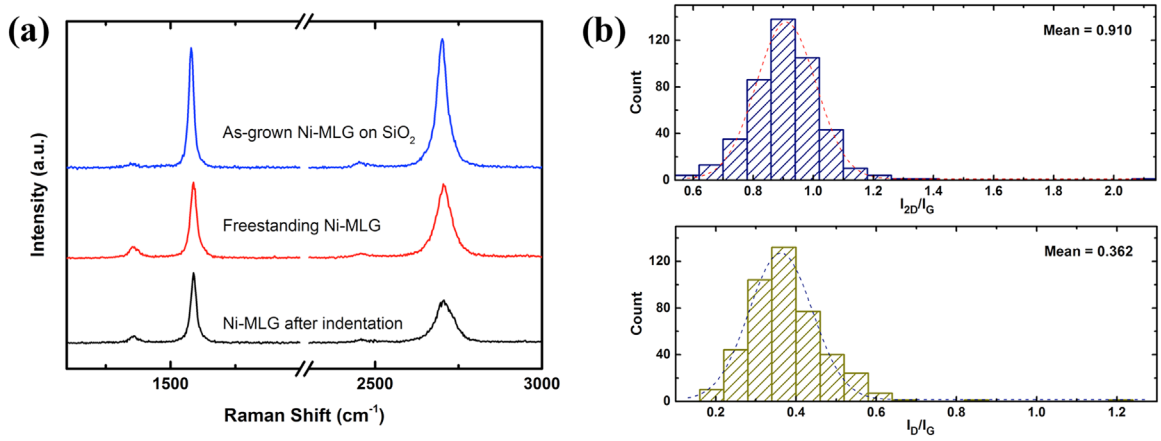

Figure 2. Raman spectra of Ni–MLG. a) Raman spectra of as-grown Ni–MLG films, freestanding Ni–MLG nanomembranes before and after indentation. b) Raman spectra histograms are obtained from spatial maps of (20 × 20 μm) area. Top panel: I_{2D}/I_G ratio is calculated by integrating the area under the curve in a). The average value of I_{2D}/I_G is 0.910, which agrees with MLG having uniform thickness. Bottom panel: I_D/I_G distribution suggests high quality MLG films.

© 2017 WILEY-VCH Verlag GmbH & Co. KGaA, Weinheim

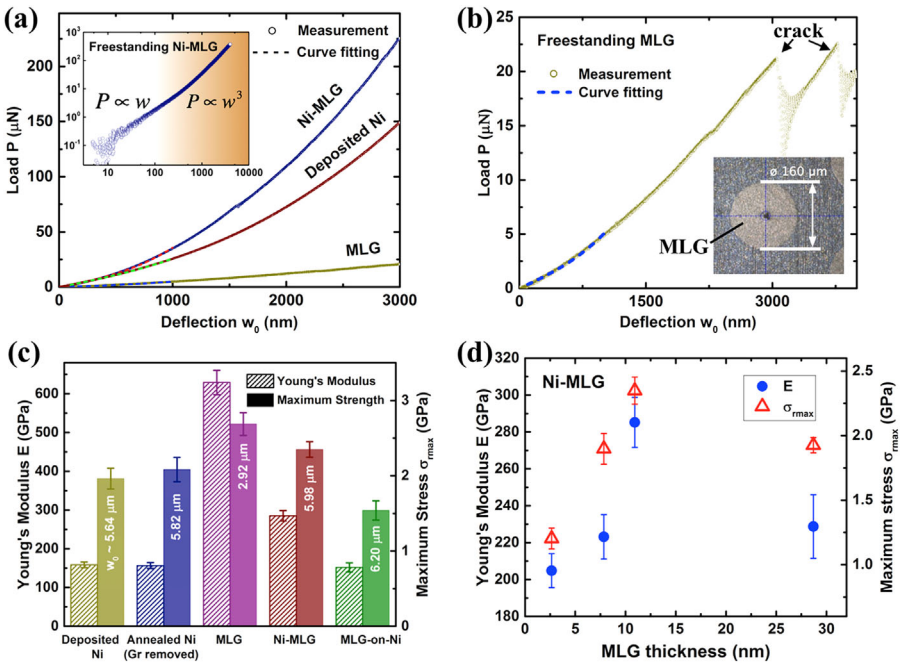

Figure 3. Mechanical behaviors of freestanding Ni–MLG membranes. a) Raw load (P)-deflection (w_0) curves for freestanding Ni–MLG, Ni, and graphene membranes. Note the difference between their thicknesses. Curve fitting using Equation 1 is used to extract the modulus, and the logscale inset plot shows the slope change transition from bending-dominated behavior to membrane stretching as deformation increases. b) Load-deflection and curve fitting for freestanding graphene thin film, where micro-cracks initiate at high deflections (>3 μm). c) Summary of the measured elastic moduli and the maximum stresses in the designed thin films, showing the strengthening observed in Ni–MLG composite membranes. The values listed within stress bars are the maximum deflections before film fracture. d) Dependence of E and σ_{rmax} on the synthesis duration and MLG thickness.

is the pretension in the clamped thin film resulting from biaxial tensile stress during fabrication process, and f_υ is the function of Poisson's ratio as $1.0491 - 0.1462\upsilon - 0.1583\upsilon^2$.[22a] Equation 1 combines plate-bending behavior within the first two linear terms and membrane stretching behavior represented by the third nonlinear term. The E and σ_0 are calculated by least square fitting of the measured load-deflection data. In our experiments, membrane deflection is large due to the large membrane radius, small indenter tip and thin thickness, thus the nonlinear term in Equation 1 turns to be more significant and govern the shape of the curves in Figure 3**a**. Notably, we verified that Equation 1 can be applied to extract and compare the homogenized properties of all of our films (Ni, MLG, and Ni–MLG) (see SI). By comparing Equation 1 with finite element method (FEM) simulations using COMSOL,[23] we verified that the difference between the homogenized composite and the multi-layered composite membranes is small compared to other variations and experimental errors, which validates the applicability of Equation 1 for the analysis (Figure S3).

To evaluate the strength of the membranes, Equation 2 is used to estimate the maximum radial stress underneath the indenter.[21,24]

$$\sigma_{rmax} = \sqrt{\frac{P_b E_t}{4\pi hc}} \tag{2}$$

where P_b is the breaking load obtained from the indentation measurement. This value corresponds to the maximum stress in the film in the case of an indenter tip having finite but small radius and frictionless interface with the film. Importantly, we replaced the elastic modulus E calculated from the elastic regime (reported earlier in the manuscript) with the homogenized tangential modulus E_t extracted by fitting in the vicinity of the breaking load. This tangential modulus accounts for the local elastoplastic deformation at high loads as described in the SI (Figure S3). SEM images shown in **Figure 4** confirm that the breakage and hence the point of maximum stress occurs at the center of the indenter tip. Notably, σ_{rmax} is independent of the indenter size or thin film diameter when $\frac{c}{a} \ll 1$.[21] Figure 3**c** and Table S1 summarize the calculated elastic moduli and the maximum stresses by curve fitting using Equation 1 and 2. The deposited Ni film has a modulus value of $\approx 158.54 \pm 7.35$ GPa, which is 79% of the bulk values of Ni (200 GPa). The discrepancy between the theoretical and calculated values can be mainly attributed to the surface roughness of the sputtered Ni films leading to difficult in estimating the exact thickness. Additionally, the tested Ni membranes, which have very large diameter to thickness ratio, include $\approx 8.6 \times 10^7$ grains. The large number of columnar grains correlates with high probability of intrinsic defects. For the free-standing MLG membranes (Ni-etched), the average properties are $E \approx 629.30 \pm 31.35$ GPa *and* $\sigma_{rmax} \approx 2.69 \pm 0.15$ GPa, which are respectively 62.9% and 2.1% of the theoretical modulus and strength of the defect-free graphene monolayer.[1a] Notably, these values are realistic for such large area membranes (ϕ160 μm) when compared to the 1 μm diameter graphene membrane used to measure the intrinsic theoretical strength of

© 2017 WILEY-VCH Verlag GmbH & Co. KGaA, Weinheim

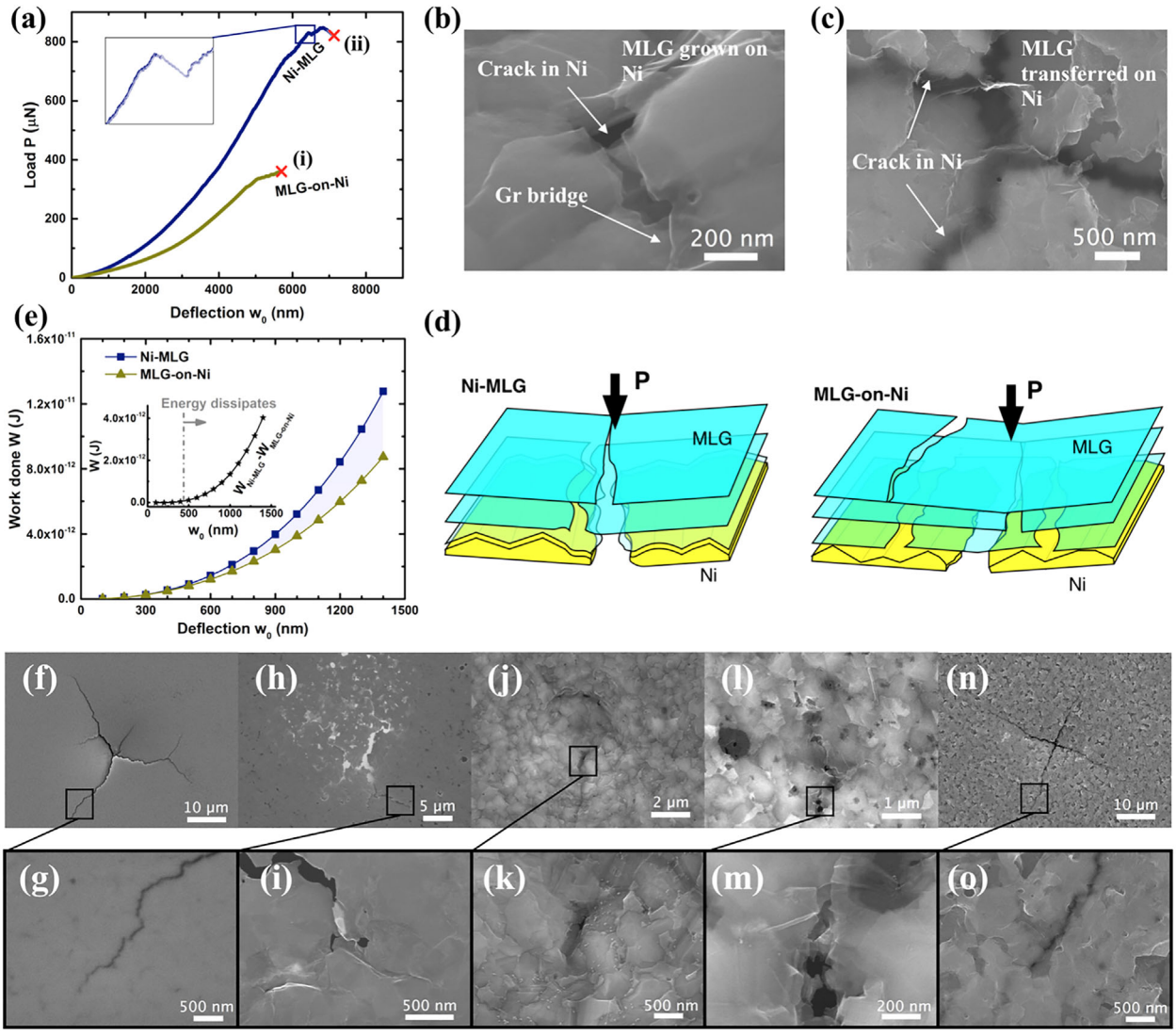

Figure 4. Strengthening mechanisms in Ni–MLG composite. a) Comparison of the load-deflection curves of Ni reinforced by in situ MLG synthesis (Ni–MLG) with Ni reinforced by MLG transfer (MLG-on-Ni). Inset shows the discontinuity due to formation of micro cracks. b) SEM images of the cracks in Ni–MLG. c) MLG-on-Ni, and d) schematics of the collocated versus the un-collocated crack mechanism. e) Indentation work during loading of the Ni–MLG and the MLG-on-Ni films by integrating load-deflection curves. Inset gives the calculated energy dissipation due to interfacial slip between Ni and MLG in a deflected Ni–MLG composite. f), g), h, i), j, k), l, m), and n, o) show SEM images of sputtered Ni (150 nm), pristine MLG, annealed Ni (control), Ni–MLG, and MLG-on-Ni films after testing.

graphene.[1a,25] In fact, we believe that the behavior of these films is more indicative measure of the expected behavior of graphene and its metal composites with realistic quality and defect densities. It is notable that at large load values, discontinuities in the load-deflection curve indicate the initiation and stable propagation of nanocracks, as shown in Figure 3**b**. We observe that the cracks do not lead to dynamic snapping of monolayer graphene. Having characterized the individual constituents, we turn to the characterization of Ni–MLG composites. In Figure 3**c**, we use the values calculated from the 10-min synthesis duration, which shows the highest mechanical performance. In this case, the MLG thickness is 10.9 nm, which corresponds to Ni–MLG composite having 7.35 vol% graphene. The average elastic modulus and the maximum stress are 285.16 ± 13.58 GPa and 2.35 ± 0.20 Gpa, respectively, representing 79.9 and 19.9% increase over those for pristine Ni, indeed confirming reinforcement beyond the rules of mixture bounds. To further understand the origin of these enhancements, we prepared Ni–MLG composite membranes by CVD synthesis as described above, then we used oxygen plasma reactive ion etching to remove the MLG (Figure 1**e**). The average strength of annealed Ni samples showed 6.1% enhancements over sputtered Ni. The difference between this enhancement, and the larger enhancement observed in the Ni–MLG samples can be contributed to carbon solid solution strengthening by carbon atoms or carbide precipitates.

© 2017 WILEY-VCH Verlag GmbH & Co. KGaA, Weinheim

Importantly, the measured Ni–MLG thin film composite has a higher strength than the value predicted by the rule of mixture based on individually testing MLG and annealed Ni, $\sigma''_{r\ expected} = \nu_{MLG}\sigma_{MLG} + \nu_{Ni}\sigma_{Ni} \approx 2.12$ GPa. The strengthening of MLG in Ni–MLG composite can be explained by the conformal interface between the MLG and the supporting Ni achieved during synthesis as depicted by Figure 1**e** and **f**. This can be understood in light of the MLG synthesis mechanism on Ni catalyst. During CVD synthesis, carbon atoms tend to dissolve in the Ni at high temperature. During fast cooling, the carbon atoms precipitate to the Ni grain boundaries and form graphene layers on the outer surface. Thus in situ synthesized MLG can conform to and bridge the grains and atomic vacancies, which could play a critical role to delaying crack initiation under external stress. Moreover, MLG can suppress dislocation motion in nano-structured metals, which enhances the yield strengthening of graphene-metal composites.[10c,14] High-resolution TEM image in Figure 1**g** also confirm that Ni–MLG composites have a remarkably smooth interface without any measurable voids or impurities.

The mechanical properties of the Ni–MLG composite with different MLG thicknesses were also investigated. Figure 3**d** shows the dependence of E and σ_{rmax} on the MLG thickness. The trend shows that the films having 10.9 nm average MLG thickness have the highest elastic modulus and strength. We use SEM, AFM, and Raman characterization to explain this trend. The characterizations confirm that the thinnest layers also do not have full MLG coverage, while the Ni–MLG composites with longest exposures to the synthesis conditions suffer from non-uniformities (Figure S7).[25–26] Accordingly, we fixed the growth time at 10 min in this study.

2.3. Toughening of Ni–MLG Composites

In addition to the elastic modulus and strength, toughness can be crucial for engineering resilient and reliable structural materials.[27] We studied the fundamental toughening mechanisms between Ni and MLG. It is known that toughness does not obey the rule of mixtures. For example, nacre and its artificial counterparts are ceramic toughened by up to an order of magnitude by a few volume % of soft low toughness polymer. Similarly, the fracture toughness of ceramics can increase by ≈235% due to the addition of 1.5 vol% graphene.[28] We indirectly measured the toughness enhancement using indentation. At large membrane deflections, the membrane fractures and nanoscale cracks can initiate and propagate as indicated by the discontinuities in load-deflection curves in Figure 4a. Using SEM imaging, we observed and compared the finite length cracks of the different films. A consistent feature observed in the fractured Ni–MLG samples (Figure 4b) is the crack bridging of the Ni film by the MLG. It is also observed that slip and pull-out between the MLG layers occur at the same location of the Ni cracks. We describe the coincident Ni cracks and MLG layer slip as collocated. On the other hand, when we transfer MLG onto the annealed Ni (designated as MLG-on-Ni control specimen, see Figure S5), the modulus and strength are less than in situ synthesized Ni–MLG composite despite having the same composition. As shown by the SEM images (Figure 4c), the fracture mechanism is also different in MLG-on-Ni compared to the Ni–MLG membranes. The cracks in the Ni film and the pull-out in MLG occur in different locations, we hence call it un-collocated crack initiation. Since the only difference between the Ni–MLG and the MLG-on-Ni is the interfacial adhesion of MLG on Ni, we explain the lower stiffness and strength of the MLG-on-Ni by taking into consideration the role of surface roughness. The van der Waals interfacial strength between MLG and Ni is expected to be governed by the contact area (which is a function of roughness). This non-uniform interfacial strength leads to the un-collocated crack nucleation depicted in Figure 4d.

To obtain more quantitative insights into the toughness of the composite films, we calculate the energy dissipation during indentation. The integration of Equation 1 leads to the work done W by indenter:

$$W = \int_0^{w_0} P(w)dw \tag{3}$$

where w is the membrane deflection and w_0 is the deflection when film fracture. W in Equation 3 presents the total energy transferred to the MLG/Ni system by indentation. It includes (i) the elastic strain energy in the Ni and MLG, (ii) the plastic strain energy in the Ni due to dislocation motion, (iii) the dissipated energy due to interlayer sliding within MLG layers, and (iv) the interfacial dissipation between MLG and Ni. Figure 4e shows the indentation work for the Ni–MLG composite as well as the MLG-on-Ni. By calculating the difference in work done between the films, $W_{Ni-MLG} - W_{MLG-on-Ni}$, which is represented by the purple region between curves, we obtain the unique evolution of energy dissipation in the Ni–MLG films. We attribute the dissipation in the Ni–MLG membranes to the higher energy required to cause interfacial slip between the Ni substrate and in situ synthesized MLG beyond the purely elastic regime ($w_0 < 0.5\ \mu$m). This is due to the more conformal contact obtained by direct in situ synthesis of MLG on metal surfaces as opposed to deposition and transfer of MLG. It has been reported that the interfacial adhesion energy of the CVD-grown MLG on Ni substrate is around 72.70 Jm^{-2}.[11] In this study, the MLG/Ni interfacial interaction in the Ni–MLG is shown as ≈20% higher than that in the MLG-on-Ni film (see Figure S5c in SI). Figure 4**f–o** shows the fractography of indented free-standing membranes. In these tests, the indenter stops and retracts when the control algorithm detects a sudden decrease in load (Figure S6). The crack advancement length and geometry can be correlated to the toughness of thin film in indentation. In sputtered Ni (Figure 4**f and g**), interganular cracks extending several microns are observed. On the other hand, the other three membranes (pristine MLG, annealed Ni and Ni–MLG) display more confined crack propagation. The MLG membrane shown in Figure 4**h and i)** also shows stable cracks compared to the dynamic crack propagation commonly observed in single crystal graphene monolayers. The crack morphologies are consistent with previous studies of relatively thick stacks of graphene oxide showing inter-layer cleavage as well as through the thickness fracture pathways.[25] Similar to fracture in graphene oxide nanosheet[25] having a high density of hydrogen bonds across the thickness,[10c] the Ni–MLG shows

© 2017 WILEY-VCH Verlag GmbH & Co. KGaA, Weinheim

a highly jagged crack path which indicates the strong load transfer between the Ni and MLG. Figure 4**l** and **m** also demonstrate limited graphene pull-out and jagged fracture surface for the MLG. The MLG-on-Ni thin film develops long straight cracks as shown in Figure 4**n** and **o**. These observations confirm the role of strong interfacial strength in achieving high strength and toughness.

We use AMFM-AFM to further explore the nanoscale surface roughness and surface modulus of the different films. This novel technique allows the measurement of not only the topography, but also the relative variation of the substrate's modulus with nanoscale spatial resolution, as-shown in **Figure 5a–h**. The measurements give relative changes in surface modulus by tracking the changes in the second resonant frequency of a multi-frequency driven cantilever.[29] The AFM images reveal that the Ni–MLG composite exhibits grain size of 200–800 nm after synthesis (Figure S1) and surface roughness of 40 nm in both cases. The MLG layers conform to the surface topography of the Ni after synthesis (Figure 5**a** and **b**). On the contrast, when MLG is transferred onto the Ni, it is mostly suspended across the peaks of the different grains due to the nanoscale Ni surface roughness, as shown in Figure 5**e** and **f**. Figure 5**j** and **l** show the surface modulus which corresponds to the topography of Figure 5**i** and **k**. Deep insights can be obtained by comparing the topography to the surface modulus for each case. The Ni grains, which possess varying moduli based on their crystal orientations, are responsible for the background fluctuations in surface modulus seen in Figure 5**c** and **d**. Moreover, the negative spikes in the surface modulus line scans can be correlated with the local MLG wrinkles, which are marked by the arrows in the topography and surface moduli image of Figure 5. However, when MLG is transferred onto the Ni, the contact is not conformal as shown in the MLG-on-Ni (Figure 5**g** and **h**). While these samples have comparable roughness, the average modulus is significantly lower than that of the synthesized conformal samples and does not reflect the expected variations in the modulus of the Ni grains due to their crystallographic orientations (Figure 5**j** and **l**). This is indicative of a suspended

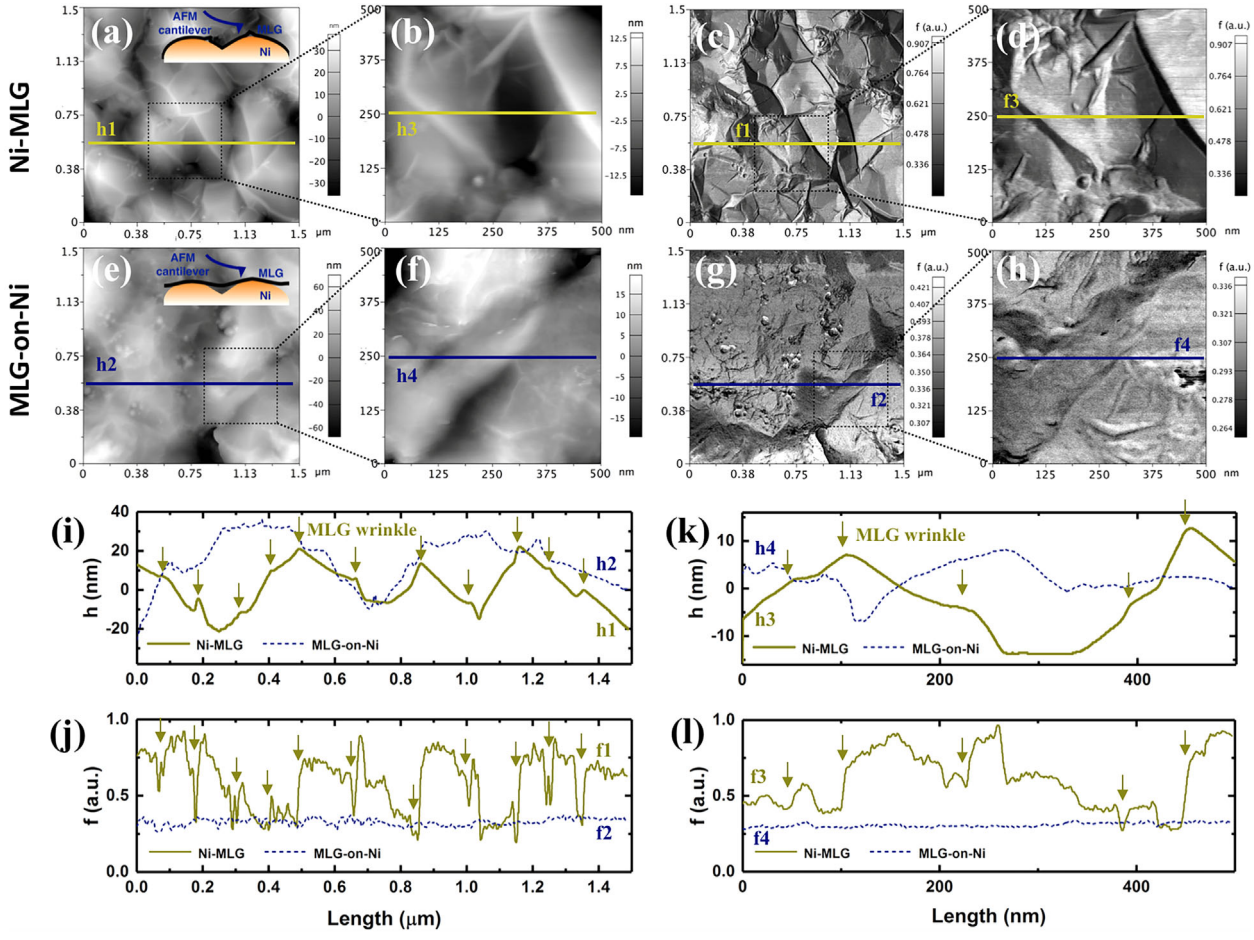

Figure 5. Amplitude Modulated Frequency Modulated Atomic Force Microscopy (AMFM-AFM) of Ni–MLG and MLG-on-Ni composites. a, b) AFM topography of Ni–MLG, c, d) relative contact stiffness of Ni–MLG from 2nd mode resonance frequency, e, f) topography of MLG-on-Ni, g, h) surface modulus of MLG-on-Ni, i) topographic line profiles along line h1 for Ni–MLG and line h2 for MLG-on-Ni, j) surface modulus profiles along line f1 (Ni–MLG) and line f2 (MLG-on-Ni), k) topographic line profiles along line h3 (Ni–MLG) and line h4 (MLG-on-Ni), l) surface modulus profiles along line f3 (Ni–MLG) and line f4 (MLG-on-Ni) (Note: arrows in i–l) point out the MLG wrinkles on in situ synthesized Ni and the corresponding softness in surface modulus).

 © 2017 WILEY-VCH Verlag GmbH & Co. KGaA, Weinheim

MLG morphology across the grains. It is reasonable to conclude that this non-conformal metal-graphene interface resulting from nanoscale surface roughness reduces the strengthening and toughening effects in the transferred MLG-on Ni samples as well as in metal-graphene composites in general.

We use the work done of nanoindentation to obtain the critical energy release rate in mode I fracture G_{Ic} for different thin films with thickness h and total crack length l_c:

$$G_{Ic} = \frac{\int_0^{w_0} P dw}{l_c h} \quad (4)^{[30]}$$

Using Equation 4, we calculate the typical fracture energy to be ≈1407 Jm^{-2} for Ni–MLG thin films. This value indicates the role of the strong MLG layer on the surface of Ni in impeding stress localization and leading to higher mechanical performance. Notably, the Ni–MLG thin films also show high electrical conductivity of 9.87×10^6 Sm^{-1}, which is slightly higher than the annealed Ni film of 9.49×10^6 Sm^{-1}. The conductivity of the MLG only is 9.62×10^7 Sm^{-1}, which is consistent to that for the aligned graphene platelets.[31] This high electrical conductivity, along with the high toughness which is over ten folds the fracture energy of thin Cu films, and other metal films, makes these composite thin films extremely attractive for use in in micro-electro-mechanical systems (MEMS) or flexible electronics, as summarized in **Figure 6**.

3. Conclusion

In summary, strengthening Ni by in situ graphene synthesis is a simple yet effective process to fabricate metal-graphene composite having strength and toughness exceeding the average properties of the constituents. This Ni–MLG composite exhibits superior mechanical and electrical properties than those of any reported metal matrix composite. With ≈7.35 vol% MLG synthesized on Ni, Young's modulus and strength are enhanced by 79.9 and 19.9% respectively. Membrane naonindentation is implemented to obtain the critical fracture energy of Ni–MLG, which is found to be 1407 Jm^{-2}, an order of magnitude higher than sputtered thin metal films. The study uses multi-frequency AFM to uncover the role of the interface in the failure of the composite, and reveals several important strengthening and toughening mechanisms. In particular, it is found that the ideal reinforcement should be conformal to the metal grains and have high interfacial strength. This enables efficient load transfer across the whole material, as well as crack bridging and energy dissipation during crack advancement leading to high toughness. This study hence promotes metal-graphene processing routes based on in situ graphene synthesis, and shows the promise of these materials to achieve very high strength surpassing the rules of mixtures.

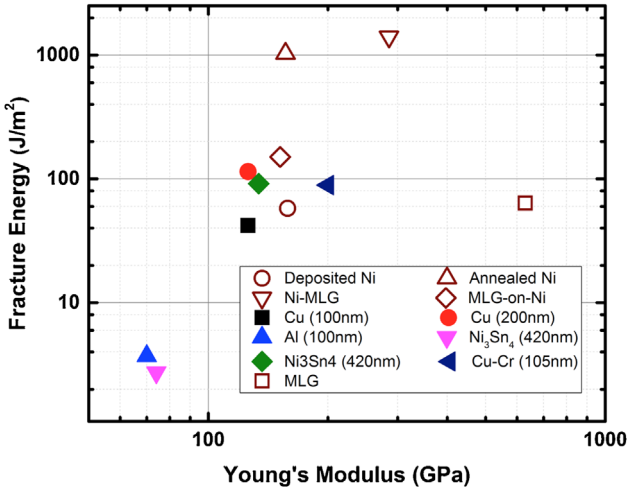

Figure 6. Summary of Modulus versus Fracture energy for Ni–MLG composite film and relevant thin metal films for MEMS and flexible electronics applications. Hollow points are the thin films tested in this study. For solid points: Cu (100 nm),[33] Cu (200 nm),[34] Al,[8a] Au,[35] Ni_3Sn_4,[36] Cu–Cr.[37]

4. Experimental Section

Free-standing thin films preparation: After synthesis, the Ni–MLG thin films (≈3 mm × 5 mm) are submerged in dionized water to delaminate them from the SiO_2/Si substrate. We use a perforated stainless steel substrate (≈130 μm thick, with ø = 160 μm holes) to receive the floating Ni–MLG thin film, followed by drying the freestanding samples at room temperature for over 24 h. To test pristine MLG samples, after floating Ni–MLG on deionized water, the solution is exchanged to the Ni etchant $FeCl_3/HCl$ and left for over 6 h, then rinsed in deionized water before being transferred to the perforated substrate. For annealed Ni samples, MLG coating was etched from a freestanding Ni–MLG thin film with a Reactive Ion Etcher (RIE) Jupiter III at condition of 100 W for 3 min in Oxygen and Argon. To fabricate the MLG-on-Ni, we first submerge an as-grown Ni–MLG thin film in deionized water to delaminate it from the SiO_2/Si substrate, then transfer the floating Ni–MLG film over the perforated substrate. After drying for 24 h at room temperature, we remove the MLG layers by RIE plasma etching. We also prepare a floating MLG film by following the procedures for pristine MLG samples. We use the suspended annealed Ni thin film to scoop up the floating MLG piece from deionized water and let it dry for another 24 h at room temperature, as shown in Figure S5a in SI. The annealed Ni and MLG come from the same batch of CVD synthesis. Therefore the overlaid MLG/Ni thin film can serve as the MLG-on-Ni sample.

Characterization of Ni–MLG composite nanomembrane: The morphology and structure of Ni–MLG thin film composites were characterized by SEM (JEOL JSM-7000F), TEM (JEOL JEM-2100 Cryo), and Confocal Raman spectroscopy (Horiba Confocal Raman microscope). For each thin film, ten indentations were conducted. The force (load) and deflection were directly measured from the Hysitron TI-950 Triboindenter using a Cono-Spherical tip (ø = 5 μm with cone angle of 60°). The transducer resolution is ≈1 nN for load and ≈0.02 nm for displacement. Load-control mode was used with pre-setting load of 2 μN and loading rate of 80 μN s^{-1} (for Ni, Ni–MLG, Annealed Ni) and 2 μN s^{-1} (for MLG).

Bimodal atomic force microscopy (AFM) images were obtained on an Asylum Research Cypher S atomic force microscope using Budget Sensors Tap300Al-G cantilevers.[32] Cantilevers were excited piezoelectrically. The cantilever was excited at its fundamental and second modes. The first mode was controlled using standard amplitude modulation (AM, or 'tapping mode'); where cantilever deflection is held constant via adjustments to the tip-sample distance. The second mode was controlled via frequency modulation (FM). The second mode excitation signal tracked the second mode resonance frequency via a phase-locked loop and maintained the constant oscillation amplitude via an automatic gain control circuit.The combination of these two imagining modes (AM-FM)

© 2017 WILEY-VCH Verlag GmbH & Co. KGaA, Weinheim

yields both topographic (first mode) and tip-sample interaction (second mode) information.

Supporting Information

Supporting Information is available from the Wiley Online Library or from the author.

Acknowledgement

All authors acknowledge funds from the department of Mechanical Science and Engineering at the University of Illinois at Urbana-Champaign. S.T. and K.Z. acknowledge partial support from US Office of Naval Research (ONR) grant N00014-15-1-2469 (Dr. Ignacio Perez). The chemical vapor deposition system is supported by funding from the Illinois Applied Research Institute (ARI).

Conflict of Interests

The authors declare no conflict of interest.

Keywords

multilayer graphene, metal-graphene composite, nanoindentation, toughness, multi-functional material

Received: June 2, 2017
Revised: July 18, 2017
Published online: August 2, 2017

[1] a) C. Lee, X.D. Wei, J.W. Kysar, J. Hone, *Science* **2008**, *321*, 385; b) K. S. Kim, Y. Zhao, H. Jang, S. Y. Lee, J. M. Kim, K. S. Kim, J. H. Ahn, P. Kim, J. Y. Choi, B. H. Hong, *Nature* **2009**, *457*, 706; c) H. X. Chang, H. K. Wu, *Adv Funct Mater* **2013**, *23*, 1984.
[2] M. L. Hammock, A. Chortos, B. C. K. Tee, J. B. H. Tok, Z. N. Bao, *Adv. Mater.* **2013**, *25*, 5997.
[3] S. S. Chen, L. Brown, M. Levendorf, W. W. Cai, S. Y. Ju, J. Edgeworth, X. S. Li, C. W. Magnuson, A. Velamakanni, R. D. Piner, J. Y. Kang, J. Park, R. S. Ruoff, *ACS Nano* **2011**, *5*, 1321.
[4] a) Y. K. Chen, X. Zhang, E. Z. Liu, C. N. He, C. S. Shi, J. J. Li, P. Nash, N. Q. Zhao, *Sci. Rep.* **2016**, *6*, 9; b) Z. Hu, G. Tong, D. Lin, C. Chen, H. Guo, J. Xu, L. Zhou, *Mater. Sci. Technol.* **2016**, *32*, 930; c) C. D. Wang, J. L. Xu, M. F. Yuen, J. Zhang, Y. Y. Li, X. F. Chen, W. J. Zhang, *Adv Funct Mater* **2014**, *24*, 6372.
[5] A. Reina, X. T. Jia, J. Ho, D. Nezich, H. B. Son, V. Bulovic, M. S. Dresselhaus, J. Kong, *Nano Lett.* **2009**, *9*, 30.
[6] a) T. Yamada, Y. Hayamizu, Y. Yamamoto, Y. Yomogida, A. Izadi-Najafabadi, D. N. Futaba, K. Hata, *Nat. Nanotechnol.* **2011**, *6*, 296; b) S. Park, M. Vosguerichian, Z. A. Bao, *Nanoscale* **2013**, *5*, 1727.
[7] a) D. Y. Khang, H. Q. Jiang, Y. Huang, J. A. Rogers, *Science* **2006**, *311*, 208; b) J. A. Rogers, T. Someya, Y. Huang, *Science* **2010**, *327*, 1603.
[8] a) M. A. Haque, M. T. A. Saif, *J. Mater. Res.* **2005**, *20*, 1769; b) J. K. Luo, A. J. Flewitt, S. M. Spearing, N. A. Fleck, W. I. Milne, *Mater. Lett.* **2004**, *58*, 2306.
[9] P. Zhang, L. L. Ma, F. F. Fan, Z. Zeng, C. Peng, P. E. Loya, Z. Liu, Y. J. Gong, J. N. Zhang, X. X. Zhang, P. M. Ajayan, T. Zhu, J. Lou, *Nat. Comm.* **2014**, *5*, 3782.
[10] a) Z. Li, G. L. Fan, Z. Q. Tan, Q. Guo, D. B. Xiong, Y. S. Su, Z. Q. Li, D. Zhang, *Nanotechnology* **2014**, *25*, 8; b) J. Hwang, T. Yoon, S. H. Jin, J. Lee, T. S. Kim, S. H. Hong, S. Jeon, *Adv. Mater.* **2013**, *25*, 6724; c) D. B. Xiong, M. Cao, Q. Guo, Z. Q. Tan, G. L. Fan, Z. Q. Li, D. Zhang, *ACS Nano* **2015**, *9*, 6934.
[11] S. Das, D. Lahiri, D. Y. Lee, A. Agarwal, W. Choi, *Carbon* **2013**, *59*, 121.
[12] B. Lim, C. J. Kim, B. Kim, U. Shim, S. Oh, B. H. Sung, J. H. Choi, S. Baik, *Nanotechnology* **2006**, *17*, 5759.
[13] R. G. Hoagland, R. J. Kurtz, C. H. H. Jr, *Scr. Mater.* **2004**, *50*, 775.
[14] Y. Kim, J. Lee, M. S. Yeom, J. W. Shin, H. Kim, Y. Cui, J. W. Kysar, J. Hone, Y. Jung, S. Jeon, S. M. Han, *Nat. Comm.* **2013**, *4*, 2114.
[15] D. Q. McNerny, B. Viswanath, D. Copic, F. R. Laye, C. Prohoda, A. C. Brieland-Shoultz, E. S. Polsen, N. T. Dee, V. S. Veerasamy, A. J. Hart, *Sci. Rep.* **2014**, *4*, 9.
[16] C. H. Lee, J. H. Kim, C. Y. Zou, I. S. Cho, J. M. Weisse, W. Nemeth, Q. Wang, A. C. T. Van Duin, T. S. Kim, X. L. Zheng, *Sci. Rep.* **2013**, *3*, 6.
[17] J. A. Robinson, M. Wetherington, J. L. Tedesco, P. M. Campbell, X. Weng, J. Stitt, M. A. Fanton, E. Frantz, D. Snyder, B. L. VanMil, G. G. Jernigan, R. L. Myers-Ward, C. R. Eddy, D. K. Gaskill, *Nano Lett.* **2009**, *9*, 2873.
[18] a) I. Childres, L. A. Jauregui, W. J. Park, H. L. Cao, Y. P. Chen, *New Dev. Photon Mater. Res.* **2013**, *1*, 20; b) L. Gong, I. A. Kinloch, R. J. Young, I. Riaz, R. Jalil, K. S. Novoselov, *Adv. Mater.* **2010**, *22*, 2694.
[19] M. M. Lucchese, F. Stavale, E. H. Martins Ferreira, C. Vilani, M. V. O. Moutinho, Rodrigo B. Capaz, C. A. Achete, A. Jorio, *Carbon* **2010**, *48*, 1592.
[20] X. D. Wei, Z. X. Meng, L. Ruiz, W. J. Xia, C. Lee, J. W. Kysar, J. C. Hone, S. Keten, H. D. Espinosa, *ACS Nano* **2016**, *10*, 1820.
[21] N. M. Bhatia, W. Nachbar, *Int. J. Nonlinear Mech.* **1968**, *3*, 307.
[22] a) U. Komaragiri, M. R. Begley, J. G. Simmonds, *J. Appl. Mech.* **2005**, *72*, 203; b) S. Hong, T. P. Weihs, J. C. Bravman, W. D. Nix, *J. Electron. Mater.* **1990**, *19*, 903; c) R.M. Jennings, J. F. Taylor, R. J. Farris, *J. Adhesion* **1995**, *49*, 57.
[23] *COMSOL Structural Mechanics Module User's Guide*, Version 5.0.1.276, December *17*, **2014**.
[24] N. M. Bhatia, W. Nachbar, *AIAA J.* **1968**, *6*, 1050.
[25] C. H. Cao, M. Daly, B. Chen, J. Y. Howe, C. V. Singh, T. Filleter, Y. Sun, *Nano Lett.* **2015**, *15*, 6528.
[26] Y. Zhang, L. Gomez, F. N. Ishikawa, A. Madaria, K. Ryu, C. A. Wang, A. Badmaev, C. W. Zhou, *J. Phys. Chem. Lett.* **2010**, *1*, 3101.
[27] R. O. Ritchie, *Nat. Mater.* **2011**, *10*, 817.
[28] a) M. A. Rafiee, J. Rafiee, I. Srivastava, Z. Wang, H. H. Song, Z. Z. Yu, N. Koratkar, *Small* **2010**, *6*, 179; b) L. S. Walker, V. R. Marotto, M. A. Rafiee, N. Koratkar, E. L. Corral, *ACS Nano* **2011**, *5*, 3182.
[29] J. R. Lozano, R. Garcia, *Phys. Rev. Lett.* **2008**, *100*, 076102.
[30] M. A. Meyers, K. K. Chawla, *Mechanical Behavior of Materials*, 2nd Edition **2009**, 1.
[31] L. T. Drzal, *Presentation: Electrical Conductivity of Aligned Graphene Nanoplatelets from XGSciences*, http://xgsciences.com/library/material-safety-data-sheets/, 2013 April.
[32] A. Labuda, M. Kocun, W. Meinhold, D. Walters, R. Proksch, *Beilstein. J. Nanotech.* **2016**, *7*, 970.
[33] H. Hirakata, O. Nishijima, N. Fukuhara, T. Kondo, A. Yonezu, K. Minoshima, *Mater. Sci. Eng. A* **2011**, *528*, 8120.
[34] R. R. Keller, J. M. Phelps, D. T. Read, *Mater. Sci. Eng. A* **1996**, *214*, 42.
[35] H. Hosokawa, A. V. Desai, M. A. Haque, *Thin Solid Films* **2008**, *516*, 6444.
[36] Z. Chen, M. He, B. Balakrisnan, C. C. Chum, *Mater. Sci. Eng. A* **2006**, *423*, 107.
[37] H. G. Kim, J. W. Yi, S. W. Kim, K. S. Kim, K. S. Kumar, *Acta Mater.* **2015**, *84*, 95.

 © 2017 WILEY-VCH Verlag GmbH & Co. KGaA, Weinheim